HHS Public Access

Author manuscript

*Nucl Med Biol*. Author manuscript; available in PMC 2016 June 01.

Published in final edited form as:

*Nucl Med Biol*. 2015 June ; 42(6): 570–577. doi:10.1016/j.nucmedbio.2014.08.003.

# Evaluation of [$^{18}$F]-(−)-Norchlorofluorohomoepibatidine ([$^{18}$F]-(−)-NCFHEB) as a PET Radioligand to Image the Nicotinic Acetylcholine Receptors in Non-human Primates

**Frederic Bois**[1], **Jean-Dominique Gallezot**[1], **Ming-Qiang Zheng**[1], **Shu-Fei Lin**[1], **Irina Esterlis**[1,2], **Kelly P. Cosgrove**[1,2], **Richard E. Carson**[1], and **Yiyun Huang**[1]

[1]PET Center, Department of Diagnostic Radiology, Yale University School of Medicine, New Haven, CT, USA

[2]Department of Psychiatry, Yale University School of Medicine, New Haven, CT, USA

## Abstract

**Introduction—**The aims of the present study were to develop an optimized microfluidic method for the production of the selective nicotinic acetylcholine $\alpha_4\beta_2$ receptor radiotracer [$^{18}$F]-(−)-NCFHEB ([$^{18}$F]-Flubatine) and to investigate its receptor binding profile and pharmacokinetic properties in rhesus monkeys *in vivo*.

**Methods—**[$^{18}$F]-(−)-NCFHEB was prepared in two steps, a nucleophilic fluorination followed by *N*-Boc deprotection. PET measurements were performed in rhesus monkeys including baseline and preblocking experiments with nicotine (0.24 mg/kg). Radiometabolites in plasma were measured using HPLC.

**Results—**[$^{18}$F]-(−)-NCFHEB was prepared in a total synthesis time of 140 min. The radiochemical purity in its final formulation was >98% and the mean specific radioactivity was 97.3 ± 16.1Bq/μmol (n = 6) at end of synthesis (EOS). In the monkey brain, radioactivity concentration was high in the thalamus, moderate in the putamen, hippocampus, frontal cortex, and lower in the cerebellum. Nicotine blocked 98–100% of [$^{18}$F]-(−)-NCFHEB specific binding, and the non-displaceable distribution volume ($V_{ND}$) was estimated at 5.9 ± 1.0 mL/cm$^3$ (n = 2), or 6.6 ± 1.1 mL/cm$^3$ after normalization by the plasma free fraction $f_P$. Imaging data are amenable to kinetic modeling analysis using the multilinear analysis (MA1) method, and model-derived binding parameters display good test-retest reproducibility. In rhesus monkeys, [$^{18}$F]-(−)-NCFHEB can yield robust regional binding potential ($BP_{ND}$) values (thalamus = 4.1 ± 1.5, frontal cortex = 1.2 ± 0.2, putamen = 0.96 ± 0.45, cerebellum = 0.10 ± 0.29).



Corresponding author: Frederic Bois, PhD. Yale PET Center, 801 Howard Avenue, New Haven, CT, 06520-8048. frederic.bois@yale.edu. Phone: 203-737-5538. Fax: 203-785-2994.

**Conclusion—**An efficient microfluidic synthetic method was developed for preparation of [$^{18}$F]-(−)-NCFHEB. PET examination in rhesus monkeys showed that [$^{18}$F]-(−)-NCFHEB entered the brain readily and its regional radioactivity uptake pattern was in accordance with the known distribution of $\alpha_4\beta_2$ receptors. Estimated non-displaceable binding potential ($BP_{ND}$) values in brain regions were better than those of [18F]-2FA and comparable to [18F]-AZAN. These results confirm previous findings and support further examination of [$^{18}$F]-(−)-NCFHEB in humans.

### Keywords

NCFHEB; Flubatine; PET; Nicotinic Acetylcholine Receptors; Rhesus monkeys; Nicotine

## 1. Introduction

Cholinergic neurotransmission in the brain depends on the integrity of nicotinic acetylcholine receptors (nAChRs), which consist of five subunits, each with four transmembrane domains for which nicotine and acetylcholine have high affinity. Dysfunction of this neuronal substrate has been implicated in Alzheimer's disease [1–3], Parkinson's disease [4, 5] and schizophrenia [6–8]. Non-invasive imaging of nAChRs using positron emission tomography (PET) or Single-Photon Emission Computed Tomography (SPECT) allows the investigation of the nAChR *in vivo* and can lead to further understanding of neuropsychiatric disorders related to cholinergic dysfunction and assist with the diagnosis of these diseases and evaluation of therapeutic agents. Over the years, various PET/SPECT radioligands such as [$^{18}$F]-2-F-A85380 ([$^{18}$F]2-FA) and [$^{123}$I]-5-I-A85380 ([$^{123}$I]5-IA) have been explored for the imaging of $\alpha_4\beta_2$*-containing nAChRs ($\alpha_4\beta_2$*-nAChRs) (Figure 1). Even though [$^{18}$F]2-FA and [$^{123}$I]5-IA have been advanced to human use [9–13], these two radiotracers suffer from some major limitations in their imaging characteristics, especially slow tissue uptake kinetics requiring long scan times (> 4 h) in order to achieve stable measurements of binding parameters. These limitations have led to the exploration of new tracers with improved imaging properties [14–18].

Recent efforts to develop a nAChR radioligand with faster brain kinetics and improved binding potential (BP) have yielded two new potential candidates. First, [$^{18}$F]AZAN (Figure 1) is an epibatidine-based nAChR antagonist that exhibits better imaging properties than those of [$^{18}$F]2-FA, including a higher brain uptake and binding potential values, faster kinetics and lower acute toxicity. A scan time of 90 min, as compared to 6 h for [$^{18}$F]2-FA, is sufficient for the reliable estimation of outcome measures. Another recent addition is [$^{18}$F]-(−)-norchlorofluorohomo-epibatidine ([$^{18}$F]-(−)-NCFHEB or [$^{18}$F]Flubatine), an antagonist derived from the high affinity homoepibatidine scaffold with the potential to image and quantify the $\alpha_4\beta_2$-nAChRs in a shorter scan time due to its rapid uptake kinetics *in vivo* [19–21]. Herein, we report the radiosynthesis of [$^{18}$F]-(−)-NCFHEB using a microfluidic reactor, and evaluation of its imaging properties in rhesus monkeys.

## 2. Materials and Methods

### 2.1. Materials

[$^{18}$F]Fluoride was produced via the $^{18}$O(p, n)$^{18}$F nuclear reaction in a GE PETtrace cyclotron (16.5-MeV protons; GE Medical Systems, Uppsala, Sweden). $H_2{}^{18}O$ was obtained

from Huayi Isotopes (Toronto, Canada). Anion exchange Chromafix cartridges (PS-$HCO_3$) for [$^{18}$F]fluoride trapping were purchased from Macherey-Nagel (Dueringen, Germany). Precursor and reference standard for [$^{18}$F]-(−)-NCFHEB were obtained from ABX Biochemicals (Radeberg, Germany). Nicotine and other reagents were purchased from Fluka or Sigma-Aldrich and used without further purification. Solid-phase extraction (SPE) cartridges (SepPak C18) were purchased from Waters Associates (Milford, MA, USA). Microfluidic reactions were carried out using an Advion NanoTek unit (Ithaca, NY, USA) with dedicated control software (Advion, version 1.4.1).

Purification of [$^{18}$F]-(−)-NCFHEB was performed by reverse phase semi-preparative HPLC using a Phenomenex Develosil C30 column (10 μm, 250 × 10 mm), eluting at a flow rate of 5 mL/min with a mobile phase composed of 10:90 (v/v) acetonitrile/0.1 N ammonium formate solution adjusted to pH = 3.5 with 12 N HCl. Quality control analyses were carried out using a Shimadzu LC-20AT Prominence HPLC system equipped with an SPD-20A UV/Vis detector (254 nm) operating in series with a Bioscan Flow-Count gamma detector (HPLC column: Phenomenex Gemini NX, 5 μm, 4.6 × 250 mm; mobile phase: 18:82 (v/v) acetonitrile/20 mM ammonium bicarbonate; flow rate: 1 mL/min].

PET scans were performed on the Focus 220 PET scanner (Siemens/CTI, Knoxville, TN, USA) with an intrinsic resolution of 1.4 mm at the center of the field of view. The radiotracer and the blocking drug nicotine were administered using an automatic syringe pump (Harvard PHD 22/2000, Harvard Apparatus, Holliston, Massachusetts, United States). Plasma separation was performed by centrifugation on an Allegra X-22R Centrifuge (Beckman Coulter, Fullerton, CA, USA). Whole blood and plasma samples were counted in a cross-calibrated well counter (Wizard 1480, Perkin Elmer, Waltham, MA, USA). Free fraction measurement was performed with ultrafiltration tubes (Centrifree UF device number 4104, Millipore, Billerica, MA, USA) by centrifugation at 1,228 g for 20 min in an IEC Medilite centrifuge (Thermo Fisher Scientific, Waltham, MA, USA).

## 2.2. Methods

**2.2.1 Chemistry—**[$^{18}$F]-(−)-NCFHEB was synthesized as described in Scheme 1. No-carrier-added [$^{18}$F]fluoride was sent to an Advion NanoTek unit (Scheme 2) where it was trapped onto a PS-$HCO_3$ anion-exchange cartridge and eluted with 0.6 mL of a Kryptofix 2.2.2 (10 mg, 53.2 μmol)/potassium carbonate (1 mg, 7.2 μmol) solution in acetonitrile/water (70:30, v/v). Azeotropic drying was performed at 110 °C by addition of 0.5 mL of acetonitrile from the pump of the CE unit. Dried [$^{18}$F]fluoride/Kryptofix 2.2.2 mixture was redissolved in anhydrous acetonitrile (450 μL). The ammonium salt precursor (0.5–1 mg) was dissolved in acetonitrile (600 μL). The two solutions were loaded and stored in their respective loops until transfer to the reactor through the transfer lines. Defined amounts of each solution were simultaneously pushed through the reactor heated at 150 °C. Upon reaction, the crude product solution was swept out of the reactor with 300 μL of acetonitrile into a v-vial. Evaporation of the acetonitrile was achieved under a stream of nitrogen at 50 °C. Subsequent addition of 250 μL of trifluoroacetic acid and reaction at 50 °C for 10 min followed by a final evaporation under a stream of nitrogen yielded the crude mixture which was diluted with 1.5 mL of mobile phase and loaded onto the semi-preparative HPLC for

purification. The product fraction eluting between 12 and 16 min was collected, diluted with DI water (50 mL) and loaded onto two Waters Classic C18 Sep-Pak cartridges in series. The Sep-Pak cartridges were washed with DI water (10 mL), then eluted with 1 mL of ethanol (USP), followed by 7 mL of USP sterile saline into a 10 mL syringe. The product solution was passed through a sterile 0.22 μm membrane filter (33 mm, MILLEX-GV, Millipore) into a vented sterile 10 mL dose vial. Analytical HPLC analysis of the final product confirmed chemical and radiochemical purities of >98% and 99%, respectively. Identity of the tracer was confirmed by co-injection with the reference standard (−)-NCFHEB. Specific activity was determined by counting an aliquot of the product in a dose calibrator for radioactivity amount, performing HPLC analysis of the aliquot and determining the mass of (−)-NCFHEB associated with the injection by comparing the corresponding UV area with a standard curve relating UV area with mass.

### 2.2.2. PET imaging

**Scan Procedures:** PET imaging experiments in 2 rhesus monkeys (3 scans each, test, retest and nicotine block) were carried out in accordance with a protocol approved by the Yale University Institutional Animal Care and Use Committee (IACUC). Animals were initially anesthetized with ketamine hydrochloride (10 mg/kg, IM), and the peripheral antimuscarinic agent glycopyrrolate (4 μg/kg, IM) was given to reduce secretions. The animals were then transported to the PET facility, intubated, and maintained on oxygen and 1.5–3% isoflurane throughout the study. A 2-h interval was allowed between ketamine administration and injection of the radiotracer. Vital signs including respiration rate, blood pressure, heart rate, and temperature were monitored continuously and recorded every 15 min, and temperature was kept constant at 37 ºC with heated water blankets. Arterial blood sampling was performed using a line inserted in a radial or femoral artery. For nicotine blocking studies (n = 2), 0.24 mg/kg of nicotine was administered using a bolus-plus-infusion protocol started 5 min before tracer injection (5 min fast bolus phase of 0.06 mg/kg followed by a 2-h constant infusion at a dose of 0.18 mg/kg)[22]. [$^{18}$F]-(−)-NCFHEB (36.7 ± 0.9 MBq) was injected as a 3-min slow bolus and list-mode data were acquired for 120 min. The injected mass was 12 ± 7 ng/kg (n = 6).

**Arterial Input Function Measurement and Metabolite Analysis:** Sequential discrete arterial blood samples were taken at 0.75, 1.5, 2.25, 3, 3.75, 4.5, 5.25, 6, 8, 10, 15, 20, 25, 30, 40, 50, 60, 75, 90, 105 and 120 min postinjection. Sample volumes ranged from 0.5 to 3 mL. Plasma was separated from blood cells by centrifugation at 2,930 g for 5 min at 4 ºC. Whole blood and plasma samples were counted in a cross-calibrated well counter (Wizard 1480, Perkin-Elmer, Waltham, MA, USA).

In order to measure the ligand metabolism in plasma, seven selected plasma samples (0.5 to 2 mL) collected at 3, 8, 15, 30, 60, 90 and 120 min postinjection were mixed with urea (with a final concentration of 8 M), and filtered through a 0.45 μm Millipore Millex-HA syringe filter (Billerica, MA, USA). The filtrate was then analyzed by reverse-phase HPLC using a modified column-switching system [23]. Up to 3 mL of filtrate was loaded on the automatic HPLC system (Shimadzu, Kyoto, Japan), and a mobile phase of 1% acetonitrile water was eluted at a flow rate 2 mL/min through the capture column self-packed with C18 sorbent

(Strata-X, Phenomenex, Torrance, CA, USA). At 4 min after sample injection the content of the capture column was back-flushed onto a Phenomenex Gemini-NX C18 analytical column (5 μm, 4.6 × 250 mm) (Torrance, CA, USA), eluting with a mobile phase consisting of 81% 20 mM ammonium bicarbonate and 19% acetonitrile (v/v) at a flow rate of 1.75 mL/min. The output of the HPLC column was connected to a fraction collector (CF-1 Fraction Collector, Spectrum Chromatography, Houston, TX, USA). Fractions were collected every two min and counted in a cross-calibrated well counter.

To correct for recovery, the ratio of the radioactivity in filtrate and plasma was obtained and fitted to an exponential rise to plateau curve ($f_F(t) = A_1 - A_2 e^{-at}$). The unchanged fraction in the filtrate was fitted to an integrated gamma function:

$$f_H(t) = a\left(1 - b\left(\int_0^{dt} e^{-u}u^{c-1}du \Big/ \int_0^{\infty} e^{-u}u^{c-1}du\right)\right)e^{-\beta t}$$

The unchanged fraction in plasma was then computed as the product of the functions $f_F$ and $f_H$, and finally the arterial input function was computed as the product of the plasma radioactivity concentration and the unchanged fraction.

Plasma free fraction estimation was performed by addition of about 740 kBq of [$^{18}$F]-(−)-NCFHEB to a blood sample drawn before radiotracer injection to produce a blood standard. After mixing and centrifugation, plasma water was separated from plasma proteins using Centrifree ultrafiltration tubes (1,228 g for 20 min). Plasma and water samples were counted in triplicate and free fraction ($f_P$) was estimated as the ratio of the mean concentration in water and plasma.

**Magnetic Resonance Imaging:** MR images were previously acquired for each rhesus monkey on a Siemens 3.0 T Trio scanner, using an extremity coil. T1-weighted images were acquired in the coronal plane with a spin echo sequence (TE = 3.34, TR = 2530, flip angle = 7°, section thickness = 0.50 mm, field-of-view = 140 mm, image matrix = 256 × 256 × 176 pixels, matrix size = 0.547 × 0.547 × 0.500 mm). Non-brain tissue was removed and the image cropped to 176 × 176 × 176 pixels using MEDx software (Medical Numerics Inc., Germantown, MD, USA) before co-registration with PET images.

**Regional Time-Activity Curve (TAC) Computation:** Dynamic scan data were binned into a sequence of 33 frames (6 × 30 sec; 3 × 1 min; 2 × 2 min; 22 × 5 min), and each frame was reconstructed with the appropriate corrections (attenuation, normalization, scatter, randoms, and deadtime), using a FORE/FBP algorithm and a Shepp filter with a cut-off frequency of 0.15 times the sampling frequency (reconstructed image resolution approximately 3.2 mm). The intrinsic resolution is the resolution measured during phantom studies, using line sources. Resolution with more complex objects, e.g. monkey head, in the scanner can be lower. Moreover, the Shepp filter used to reduce the noise will also lower the resolution, and the 3.2 mm is an estimation of the effective scanner resolution with that filter.

Regional TACs were computed using a template of regions, defined on a template brain (a representative MR image of a brain, from an animal not included in the study) for the

cerebellum (5.9 $cm^3$), caudate (0.43 $cm^3$), putamen (0.38 $cm^3$), brainstem (1.9 $cm^3$), hippocampus (0.32 $cm^3$), occipital (5.2 $cm^3$), frontal (2.5 $cm^3$) and temporal (3.2 $cm^3$) cortices, and the thalamus (0.25 $cm^3$). To apply these regions of interest (ROIs) to the PET images, two coregistration transforms were estimated. First, a non-linear transformation was used (Bioimagesuite program; version 2.5; http://www.bioimagesuite.org/) between the template MRI and the MR image of each animal. This nonlinear coregistration algorithm is based on the method proposed by Rueckert *et al* [24] with modifications [25]. Then, the MR and PET images of each monkey were coregistered using a rigid body registration using an automatically-selected PET summed image [26].

**Kinetic Modeling:** The primary outcome measure for this study was the total volume of distribution ($V_T$ or $V_T/f_P$) (mL · $cm^{-3}$) [27]. Three modeling methods were used for the kinetic analysis of regional TACs: 1-Tissue (1T) and 2-Tissue (2T) compartment models [28] and multi-linear analysis (MA1) (t* = 30 min) [29], using the arterial input function. Data were weighted in the fits using an approximation of noise-equivalent counts for each frame [30]. The models were evaluated in terms of quality of fit to the data and percent standard error (%SE), where %SE=SE/$V_T$ × 100, and SE is the estimated parameter standard error calculated from the inverse of the Fisher information matrix [31]. Fit quality was compared between 1T and 2T models using the *F* test.

The test-retest variability of the volumes of distribution, $V_T$ or $V_T/f_P$, was computed as the average across animal of $2 \times \frac{\left|V_T^{Retest} - V_T^{Test}\right|}{V_T^{Retest} + V_T^{Test}}$ or $2 \times \frac{\left|\left(\frac{V_T}{f_P}\right)^{Retest} - \left(\frac{V_T}{f_P}\right)^{Test}\right|}{\left(\frac{V_T}{f_P}\right)^{Retest} + \left(\frac{V_T}{f_P}\right)^{Test}}$.

Percent change in $V_T$ (%Δ$V_T$) from baseline to post-Nicotine was computed as

$$\%\Delta V_T = \left(\frac{V_T\,(\text{Nicotine})}{V_T\,(\text{Baseline})} - 1\right) \times 100$$

[$^{18}$F]-(−)-NCFHEB non-displaceable distribution volume ($V_{ND}$) [27] was estimated using the occupancy plot [32] and [$^{18}$F]-(−)-NCFHEB binding potential $BP_{ND}$ [27] was computed as $V_T/V_{ND}-1$.

## 3. Results

### Chemistry

[$^{18}$F]-(−)-NCFHEB was synthesized using the NanoTek microfluidic system followed by acidic cleavage of the protecting group (Scheme 1). The final product was purified by semi-preparative HPLC, and formulated as a sterile and pyrogen-free isotonic solution for injection. [$^{18}$F]-(−)-NCFHEB was prepared in >98% radiochemical purity and specific activity of 97.3 ± 16.1 GBq/μmol at the end of synthesis (EOS) (range of 65.8 – 120.2 GBq/μmol, n = 6). The total synthesis time including HPLC separation, SepPak purification and formulation was ~ 140 min.

## Plasma analysis

In rhesus monkey, the radiotracer was metabolized fairly quickly, with ~43% of parent fraction remaining at 30 min following tracer injection, which decreased further to ~14% at 120 min (Fig. 2). Administration of nicotine did not have a substantial effect on radiotracer metabolism. Plasma free fraction was high at 88.0 ±1.6 % (n = 6).

## Brain imaging

After a bolus injection of [$^{18}$F]-(−)-NCFHEB in rhesus monkey, substantial uptake of radioactivity was observed in the brain regions enriched with $\alpha_4\beta_2$ nAChRs as previously described [21] (Fig. 3–4). Tissue kinetics was rapid, with peak uptake time of ~10 min in most brain regions and ~45 min in the thalamus (Fig. 3–4). The distribution of radioactivity in the brain was heterogeneous. The highest level was observed in the thalamus, intermediate level in the cortex, and the lowest level in the cerebellum (Fig. 4), in a pattern consistent with the distribution of nAChR in rhesus monkey brain. When the animals were treated with nicotine at a dose of 0.24 mg/kg, radioactivity uptake in the thalamus and cortex decreased to a level similar to that in the cerebellum (Fig. 3–4).

Regional TACs were first analyzed using 1T or 2T kinetic models. Visually better fits were obtained with the 2T model in all regions. According to the F-test, the 2T-model was significantly better in all cases (the minimum $F_{2,29}$ statistic across all regions and studies was 21.1, which correspond to a p-value of $< 10^{-5}$). However the 2T model did not provide reliable $V_T$ estimates in many cases (for 21 out of 54 fits, the relative standard error was >100%). Therefore, the multilinear analysis MA1 [33], which is based on the Logan graphical analysis, was used to achieve a better trade-off between accuracy of fits and stability of parameter estimates. With MA1 (t* = 30 min), the maximal relative standard error of $V_T$ estimates was < 4%. For the subset of data with reliable $V_T$ estimates from the 2T model (i.e., with rSE < 20%), the 2T and MA1 $V_T$ estimates were well correlated (slope of regression line = 0.953, intercept = −1.007, $r^2 = 0.974$). Regional $V_T$ estimated with MA1 from the baseline and blocking scans are listed in Table 1. [$^{18}$F]-(−)-NCFHEB $V_T$ values are 6.4 ± 1.0, 12 ± 1.0, 13 ± 1.7, and 29 ± 4.9 mL/cm$^3$, respectively, in the cerebellum, hippocampus, frontal cortex, and thalamus (n = 4). After normalization by the plasma free fraction $f_P$, $V_T/f_P$ values were 7.4 ± 1.1, 13 ± 1.1, 15 ± 1.9 and 33 ± 5.5 mL/cm$^3$, respectively, in the cerebellum, hippocampus, frontal cortex, and thalamus (n = 4) (table 1).

Test-retest variability results for the volumes of distribution $V_T$ and $V_T/f_P$ are presented in Table 2. The average test-retest variability across all ROIs was 14% for $V_T$ and slightly lower for $V_T/f_P$ (13%).

The effect of nicotine on [$^{18}$F]-(−)-NCFHEB binding was analyzed by the occupancy plot [32], using either volume of distribution $V_T$ (data not shown) or the normalized volume of distribution $V_T/f_P$ (Fig. 5). With both volumes of distribution, the occupancy plot was almost perfectly linear ($r^2 > 0.98$), indicating that the data were compatible with the hypotheses of the occupancy plot (common drug occupancy and non-displaceable volume of distribution in all ROIs). The occupancy of the target receptors by nicotine was 99.5 ± 1.4% (n = 2), indicating that at a dose of 0.24 mg/kg, nicotine completely blocked the specific binding of

[$^{18}$F]-(−)-NCFHEB in the monkey brain. From the occupancy plots the non-displaceable volume of distribution ($V_{ND}$) was estimated at 5.9 ± 1.0 mL/cm$^3$, and 6.6 ± 1.1 mL/cm$^3$ for $V_{ND}/f_P$. These $V_{ND}$ and $V_{ND}/f_P$ estimates were 8 ± 25% and 10 ± 23% lower, respectively, than the volumes of distribution $V_T$ and $V_T/f_P$ in the cerebellum, suggesting that cerebellum has some specific binding and this region may not be a perfect reference region for [$^{18}$F]-(−)-NCFHEB in rhesus monkey.

Based on the derived $V_{ND}$ values, [$^{18}$F]-(−)-NCFHEB binding potential ($BP_{ND}$), characterizing the specific receptor binding, would be ~4.1 in the thalamus, ~1 in the basal ganglia and 0.68–1.2 in the cortex (Table 1).

## 4. Discussion

Microfluidic technology has recently emerged as an efficient, automated process for the production of PET drugs with short-lived isotopes (such F-18, $t_{1/2}$ = 109.7 min) [34–36]. Compared to other automated methodologies, PET microfluidic technology provides the unique capability to conduct multiple F-18 radiolabeling trials from a single batch of radioisotope, which can lead to a dramatically shortened time for process development. Once optimized, the strictly defined production parameters inherently yield a high degree of reproducibility, essential for the routine production of F-18 PET drugs as well as improved target radiochemical and chemical purities thanks to the small amount of precursors, reagents and solvents used. We capitalized on this recent technology to develop a partially automated synthesis of [$^{18}$F]-(−)-NCFHEB. This process parallels the recent published procedures [37, 38], with an automated radiolabeling of an ammonium salt followed by a manual deprotection of the Boc protective group, but offers the key advantage to produce multiple doses hours apart from a single bombardment. Regular automated modules use the entire amount of F-18 radioactivity to produce a single dose of a particular PET drug and require cleaning between productions, therefore reducing the possible number of daily runs for this particular PET drug. Microfluidic systems can produce multiple F-18 doses by using partial amounts of the initial target output. The specific activity obviously decreases with subsequent doses, but current cyclotrons yield specific activities high enough to allow injection hours apart.

[$^{18}$F]-(−)-NCFHEB has recently emerged as a potential candidate to image the $\alpha_4\beta_2$-nAChRs thanks to its binding selectivity *in vitro* and rapid uptake kinetics *in vivo* [19–21, 37, 39]. We decided to further characterize this radiotracer's pharmacokinetic and receptor binding profiles in rhesus monkeys before its translation to human studies.

The main goals of this study were to develop an efficient, reliable method of radiosynthesis for [$^{18}$F]-(−)-NCFHEB, to evaluate [$^{18}$F]-(−)-NCFHEB brain kinetic properties in baseline and nicotine blocking studies in rhesus monkey brains, and to test various models for quantification of [$^{18}$F]-(−)-NCFHEB binding parameters. Our findings confirm the results previously obtained in pigs [19] and rhesus monkeys [21], and indicate that [$^{18}$F]-(−)-NCFHEB is suitable for imaging and quantification of $\alpha_4\beta_2$-nAChR binding in rhesus monkeys *in vivo* and present certain advantages over [$^{18}$F]2-FA. This conclusion is drawn from the following observations: The values of $BP_{ND}$ observed in different brain regions

followed the known distribution of $\alpha_4\beta_2$-like nAChRs in monkey brain [40] and were highest in the thalamus, moderate in the cortex and striatum, and lowest in the cerebellum. Estimated $V_T$ values were characterized by reasonable reproducibility with a 14% average variability for all regions in test-retest scans and 13% after normalization for free fraction. We observed no visible pharmacological effects of [$^{18}$F]-(−)-NCFHEB (i.e., no changes in heart rate, EKG and $O_2$ saturation) at doses up to 1.2 nmol/kg in rhesus monkeys.

Comparison between [$^{18}$F]-(−)-NCFHEB and [$^{18}$F]-2-FA kinetic properties in rhesus monkey [41, 42] and [$^{18}$F]-AZAN in baboon [18] brains demonstrated comparable or preferable *in vivo* binding properties of the new radioligand. Setting aside potential species differences, in the non-human primate brain, [$^{18}$F]-(−)-NCFHEB displayed faster kinetics than [$^{18}$F]-2-FA, but apparently slower than [$^{18}$F]-AZAN (Figure 4), with peak uptake of ~45 min in the thalamus (vs. ~70 min for [$^{18}$F]-2-FA, and 15–20 min for [$^{18}$F]-AZAN). The uptake of [$^{18}$F]-(−)-NCFHEB in the thalamus of rhesus monkeys was higher than any other region and then slowly cleared compared with other brain regions, which is in accordance with previous rhesus monkey results [21]. All the other brain regions peaked at ~10–15 min and decreased steadily thereafter. The clinical use of [$^{18}$F]2-FA is hindered by its slow kinetics. The graphical analysis to quantify [$^{18}$F]-2FA specific binding is region dependent and scan times of no less than 95, 175 and 275 min, respectively are required for the cerebellum, cortex and thalamus in rhesus monkeys [42] and >150 min in humans for all regions [43]. The time needed to reach equilibrium in a bolus plus infusion protocol with [$^{18}$F]-2FA was even longer, as is usually the case (~360 min in humans) [11]. [$^{18}$F]-AZAN was shown to provide reasonable estimates of $V_T$ in all brain regions within 90 min post-injection. Our initial human studies (unpublished data) indicate that an acquisition time of ~150 min is sufficient to obtain stable outcome measures with [$^{18}$F]-(−)-NCFHEB.

Model assessment selected MA1 as the method of choice for analysis of regional TACs and calculation of regional $V_T$. Nicotine at a dose of 0.24 mg/kg substantially reduced $V_T$ in all brain regions (with the exception of cerebellum), and resulted in minimal differences in uptake among brain regions. The non-displaceable volume of distribution ($V_{ND}$) of [$^{18}$F]-(−)-NCFHEB was estimated to be 5.9 ± 1.0 mL/cm$^3$, and 6.6±1.1 mL/cm$^3$ after normalizing by $f_P$. To obtain a measure of specific binding signals, regional $BP_{ND}$ values were calculated using this estimated $V_{ND}$ and regional $V_T$ values from baseline scans. These findings confirm that [$^{18}$F]-(−)-NCFHEB yields $BP_{ND}$ values comparable to those of [$^{18}$F]-AZAN and better than those of [$^{18}$F]-2-FA in the non-human primate brain.

## Conclusion

We successfully synthesized the novel nAChR radiotracer [$^{18}$F]-(−)-NCFHEB using the NanoTek microfluidic reactor. Evaluation in rhesus monkey confirmed that [$^{18}$F]-(−)-NCFHEB satisfies the major requirements for a radioligand to be used for *in vivo* receptor imaging, such as feasibility to radiolabel with high specific activity, low level of binding with plasma proteins, ability to cross the blood-brain barrier and accumulate in brain regions enriched with the $\alpha_4\beta_2$-nAChRs, reversible binding characteristics, and high ratio of specific to non-specific binding. Imaging data are amenable to kinetic modeling analysis using the MA1 method, and model-derived binding parameters display good test-retest

reproducibility. Taken together, these results suggest that [$^{18}$F]-(−)-NCFHEB may have advantages over existing radiotracers for imaging the $\alpha_4\beta_2$ nAChR, and its evaluation in humans is underway.

## Acknowledgments

The authors thank the staff of the Yale University PET Center for their technical expertise and support. Supported by the VA PTSD Center and NIDA (K02DA031750). This publication was also made possible by CTSA Grant Number UL1 RR024139 from the National Center for Research Resources (NCRR), a component of the National Institutes of Health (NIH), and NIH roadmap for Medical Research.

## References

1. Martin-Ruiz CM, Haroutunian VH, Long P, Young AH, Davis KL, Perry EK, et al. Dementia rating and nicotinic receptor expression in the prefrontal cortex in schizophrenia. Biological psychiatry. 2003; 54:1222–33. [PubMed: 14643090]
2. Freedman R, Hall M, Adler LE, Leonard S. Evidence in postmortem brain tissue for decreased numbers of hippocampal nicotinic receptors in schizophrenia. Biological psychiatry. 1995; 38:22–33. [PubMed: 7548469]
3. Breese CR, Lee MJ, Adams CE, Sullivan B, Logel J, Gillen KM, et al. Abnormal regulation of high affinity nicotinic receptors in subjects with schizophrenia. Neuropsychopharmacology: official publication of the American College of Neuropsychopharmacology. 2000; 23:351–64. [PubMed: 10989262]
4. Coyle JT, Price DL, DeLong MR. Alzheimer's disease: a disorder of cortical cholinergic innervation. Science. 1983; 219:1184–90. [PubMed: 6338589]
5. Warpman U, Nordberg A. Epibatidine and ABT 418 reveal selective losses of alpha 4 beta 2 nicotinic receptors in Alzheimer brains. Neuroreport. 1995; 6:2419–23. [PubMed: 8747166]
6. Olanow CW, Tatton WG. Etiology and pathogenesis of Parkinson's disease. Annual review of neuroscience. 1999; 22:123–44.
7. Quik M, Bordia T, O'Leary K. Nicotinic receptors as CNS targets for Parkinson's disease. Biochemical pharmacology. 2007; 74:1224–34. [PubMed: 17631864]
8. D'Souza DC, Esterlis I, Carbuto M, Krasenics M, Seibyl J, Bois F, et al. Lower β2*-nicotinic acetylcholine receptor availability in smokers with schizophrenia. The American journal of psychiatry. 2012; 169:326–34. [PubMed: 22193533]
9. Saricicek A, Esterlis I, Maloney KH, Mineur YS, Ruf BM, Muralidharan A, et al. Persistent beta2*-nicotinic acetylcholinergic receptor dysfunction in major depressive disorder. The American journal of psychiatry. 2012; 169:851–9. [PubMed: 22772158]
10. Cosgrove KP, Esterlis I, McKee SA, Bois F, Seibyl JP, Mazure CM, et al. Sex differences in availability of beta2*-nicotinic acetylcholine receptors in recently abstinent tobacco smokers. Archives of general psychiatry. 2012; 69:418–27. [PubMed: 22474108]
11. Kimes AS, Chefer SI, Matochik JA, Contoreggi CS, Vaupel DB, Stein EA, et al. Quantification of nicotinic acetylcholine receptors in the human brain with PET: bolus plus infusion administration of 2-[18F]F-A85380. NeuroImage. 2008; 39:717–27. [PubMed: 17962044]
12. Gallezot JD, Bottlaender MA, Delforge J, Valette H, Saba W, Dolle F, et al. Quantification of cerebral nicotinic acetylcholine receptors by PET using 2-[18F]fluoro-A-85380 and the multiinjection approach. Journal of cerebral blood flow and metabolism: official journal of the International Society of Cerebral Blood Flow and Metabolism. 2008; 28:172–89.
13. Esterlis I, Hannestad JO, Perkins E, Bois F, D'Souza DC, Tyndale RF, et al. Effect of a nicotine vaccine on nicotine binding to beta2*-nicotinic acetylcholine receptors in vivo in human tobacco smokers. The American journal of psychiatry. 2013; 170:399–407. [PubMed: 23429725]
14. Ding YS, Fowler J. New-generation radiotracers for nAChR and NET. Nuclear medicine and biology. 2005; 32:707–18. [PubMed: 16243646]

15. Horti AG, Gao Y, Kuwabara H, Dannals RF. Development of radioligands with optimized imaging properties for quantification of nicotinic acetylcholine receptors by positron emission tomography. Life sciences. 2010; 86:575–84. [PubMed: 19303028]
16. Pichika R, Kuruvilla SA, Patel N, Vu K, Sinha S, Easwaramoorthy B, et al. Nicotinic alpha4beta2 receptor imaging agents. Part IV. Synthesis and biological evaluation of 3-(2-(S)-3,4-dehydropyrrolinyl methoxy)-5-(3′-(1)(8)F-fluoropropyl)pyridine ((1)(8)F-Nifrolene) using PET. Nuclear medicine and biology. 2013; 40:117–25. [PubMed: 23141552]
17. Pichika R, Easwaramoorthy B, Christian BT, Shi B, Narayanan TK, Collins D, et al. Nicotinic alpha4beta2 receptor imaging agents. Part III. Synthesis and biological evaluation of 3-(2-(S)-azetidinylmethoxy)-5-(3′-18F-fluoropropyl)pyridine (18F-nifzetidine). Nuclear medicine and biology. 2011; 38:1183–92. [PubMed: 21831652]
18. Kuwabara H, Wong DF, Gao Y, Valentine H, Holt DP, Ravert HT, et al. PET Imaging of nicotinic acetylcholine receptors in baboons with 18F-AZAN, a radioligand with improved brain kinetics. Journal of nuclear medicine: official publication, Society of Nuclear Medicine. 2012; 53:121–9.
19. Brust P, Patt JT, Deuther-Conrad W, Becker G, Patt M, Schildan A, et al. In vivo measurement of nicotinic acetylcholine receptors with [18F]norchloro-fluoro-homoepibatidine. Synapse. 2008; 62:205–18. [PubMed: 18088060]
20. Deuther-Conrad W, Patt JT, Lockman PR, Allen DD, Patt M, Schildan A, et al. Norchloro-fluoro-homoepibatidine (NCFHEB) - a promising radioligand for neuroimaging nicotinic acetylcholine receptors with PET. European neuropsychopharmacology: the journal of the European College of Neuropsychopharmacology. 2008; 18:222–9. [PubMed: 17728108]
21. Hockley BG, Stewart MN, Sherman P, Quesada C, Kilbourn MR, Albin RL, et al. (−)-[(18)F]Flubatine: evaluation in rhesus monkeys and a report of the first fully automated radiosynthesis validated for clinical use. J Labelled Comp Radiopharm. 2013; 56:595–9. [PubMed: 24285235]
22. Gallezot JD, Kloczynski T, Weinzimmer D, Labaree D, Zheng MQ, Lim K, et al. Imaging nicotine- and amphetamine-induced dopamine release in rhesus monkeys with [(11)C]PHNO vs [(11)C]raclopride PET. Neuropsychopharmacology: official publication of the American College of Neuropsychopharmacology. 2014; 39:866–74. [PubMed: 24220025]
23. Hilton J, Yokoi F, Dannals RF, Ravert HT, Szabo Z, Wong DF. Column-switching HPLC for the analysis of plasma in PET imaging studies. Nucl Med Biol. 2000; 27:627–30. [PubMed: 11056380]
24. Rueckert D, Sonoda LI, Hayes C, Hill DLG, Leach MO, Hawkes DJ. Nonrigid registration using free-form deformations: application to breast MR images. Medical Imaging, IEEE Transactions on. 1999; 18:712–21.
25. Papademetris X, Jackowski AP, Schultz RT, Staib LH, Duncan JS. Integrated Intensity and Point-Feature Nonrigid Registration. Med Image Comput Comput Assist Interv. 2001; 3216:763–70. [PubMed: 20473359]
26. Sandiego CM, Weinzimmer D, Carson RE. Optimization of PET-MR registrations for nonhuman primates using mutual information measures: a Multi-Transform Method (MTM). Neuroimage. 2013; 64:571–81. [PubMed: 22926293]
27. Innis RB, Cunningham VJ, Delforge J, Fujita M, Gjedde A, Gunn RN, et al. Consensus nomenclature for in vivo imaging of reversibly binding radioligands. J Cereb Blood Flow Metab. 2007; 27:1533–9. [PubMed: 17519979]
28. Gunn RN, Gunn SR, Cunningham VJ. Positron emission tomography compartmental models. Journal of Cerebral blood flow and metabolism. 2001; 21:635–52. [PubMed: 11488533]
29. Ichise M, Toyama H, Innis RB, Carson RE. Strategies to improve neuroreceptor parameter estimation by linear regression analysis. Journal of Cerebral blood flow and metabolism. 2002; 22:1271–81. [PubMed: 12368666]
30. Pajevic S, Daube-Witherspoon ME, Bacharach SL, Carson RE. Noise characteristics of 3-D and 2-D PET images. IEEE transactions on medical imaging. 1998; 17:9–23. [PubMed: 9617904]
31. Delforge J, Syrota A, Mazoyer BM. Identifiability analysis and parameter identification of an in vivo ligand-receptor model from PET data. IEEE transactions on bio-medical engineering. 1990; 37:653–61. [PubMed: 2394453]

32. Cunningham VJ, Rabiner EA, Slifstein M, Laruelle M, Gunn RN. Measuring drug occupancy in the absence of a reference region: the Lassen plot re-visited. Journal of cerebral blood flow and metabolism: official journal of the International Society of Cerebral Blood Flow and Metabolism. 2010; 30:46–50.
33. Ichise M, Toyama H, Innis RB, Carson RE. Strategies to improve neuroreceptor parameter estimation by linear regression analysis. J Cereb Blood Flow Metab. 2002; 22:1271–81. [PubMed: 12368666]
34. Dewkar GK, Sundaresan G, Lamichhane N, Hirsch J, Thadigiri C, Collier T, et al. Microfluidic radiosynthesis and biodistribution of [18 F] 2-(5-fluoro-pentyl)-2-methyl malonic acid. J Labelled Comp Radiopharm. 2013; 56:289–94. [PubMed: 24285373]
35. Kealey S, Plisson C, Collier TL, Long NJ, Husbands SM, Martarello L, et al. Microfluidic reactions using [11C]carbon monoxide solutions for the synthesis of a positron emission tomography radiotracer. Organic & biomolecular chemistry. 2011; 9:3313–9. [PubMed: 21437342]
36. Bouvet VR, Wuest M, Wiebe LI, Wuest F. Synthesis of hypoxia imaging agent 1-(5-deoxy-5-fluoro-alpha-D-arabinofuranosyl)-2-nitroimidazole using microfluidic technology. Nuclear medicine and biology. 2011; 38:235–45. [PubMed: 21315279]
37. Fischer S, Hiller A, Smits R, Hoepping A, Funke U, Wenzel B, et al. Radiosynthesis of racemic and enantiomerically pure (−)-[18F]flubatine--a promising PET radiotracer for neuroimaging of alpha4beta2 nicotinic acetylcholine receptors. Applied radiation and isotopes: including data, instrumentation and methods for use in agriculture, industry and medicine. 2013; 74:128–36.
38. Patt M, Schildan A, Habermann B, Fischer S, Hiller A, Deuther-Conrad W, et al. Fully automated radiosynthesis of both enantiomers of [18F]Flubatine under GMP conditions for human application. Applied radiation and isotopes: including data, instrumentation and methods for use in agriculture, industry and medicine. 2013; 80:7–11.
39. Deuther-Conrad W, Patt JT, Feuerbach D, Wegner F, Brust P, Steinbach J. Norchloro-fluoro-homoepibatidine: specificity to neuronal nicotinic acetylcholine receptor subtypes in vitro. Farmaco. 2004; 59:785–92. [PubMed: 15474055]
40. Cimino M, Marini P, Fornasari D, Cattabeni F, Clementi F. Distribution of nicotinic receptors in cynomolgus monkey brain and ganglia: localization of alpha 3 subunit mRNA, alpha-bungarotoxin and nicotine binding sites. Neuroscience. 1992; 51:77–86. [PubMed: 1465189]
41. Chefer SI, Horti AG, Lee KS, Koren AO, Jones DW, Gorey JG, et al. In vivo imaging of brain nicotinic acetylcholine receptors with 5-[123I]iodo-A-85380 using single photon emission computed tomography. Life sciences. 1998; 63:PL355–60. [PubMed: 9870715]
42. Chefer SI, London ED, Koren AO, Pavlova OA, Kurian V, Kimes AS, et al. Graphical analysis of 2-[18F]FA binding to nicotinic acetylcholine receptors in rhesus monkey brain. Synapse. 2003; 48:25–34. [PubMed: 12557269]
43. Gallezot JD, Bottlaender M, Gregoire MC, Roumenov D, Deverre JR, Coulon C, et al. In vivo imaging of human cerebral nicotinic acetylcholine receptors with 2-18F-fluoro-A-85380 and PET. Journal of nuclear medicine: official publication, Society of Nuclear Medicine. 2005; 46:240–7.

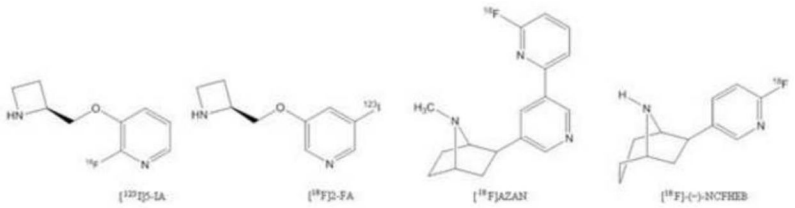


**Figure 1.**
Representative radioligands for nAChR.

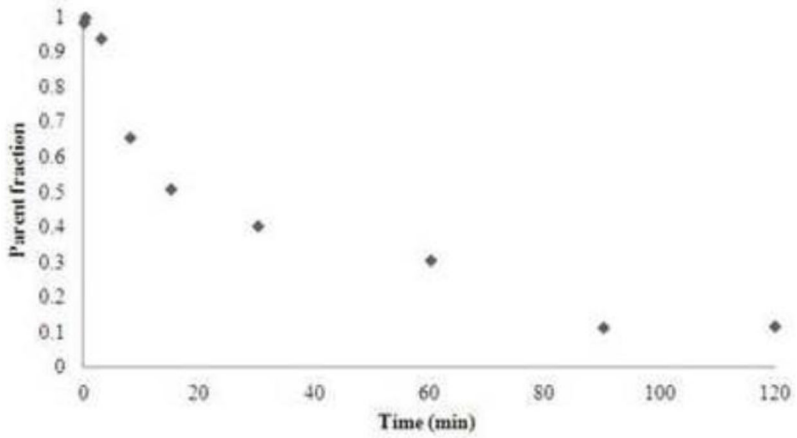


**Figure 2.**

Unmetablized fraction of [$^{18}$F]-(−)-NCFHEB in plasma after i.v bolus injection in rhesus monkey.

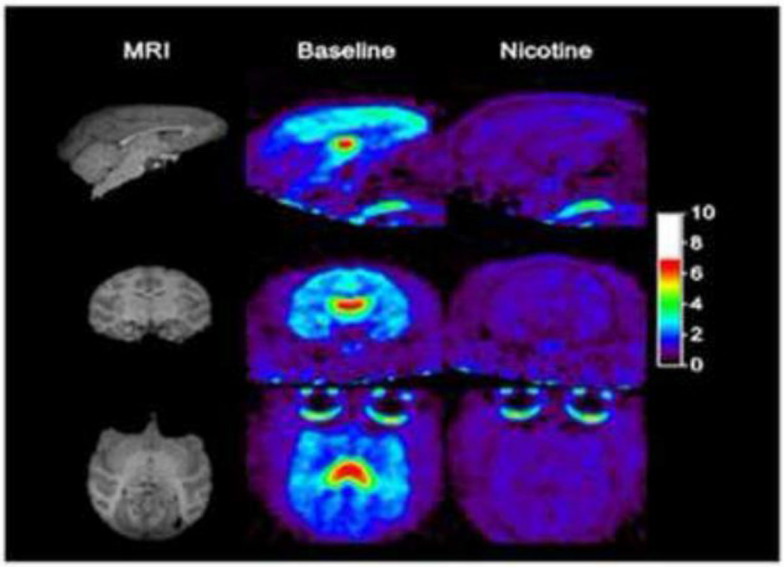


**Figure 3.**
SUV images, from 60–90 min post-injection, at baseline and after nicotine blockade.

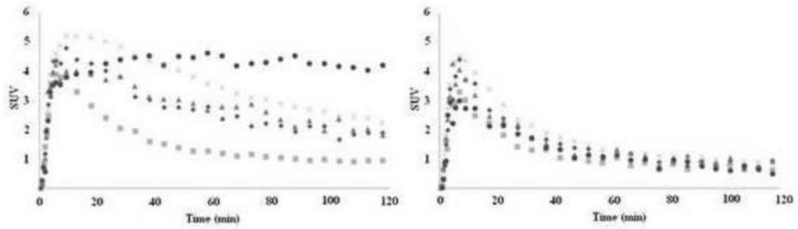


**Figure 4.**

[$^{18}$F]-(−)-NCFHEB regional time-activity curves from a baseline scan (left) and after nicotine (0.24 mg/kg) (right), in cerebellum (squares), putamen (diamonds), hippocampus (triangles), frontal cortex (cross), and thalamus (circle).

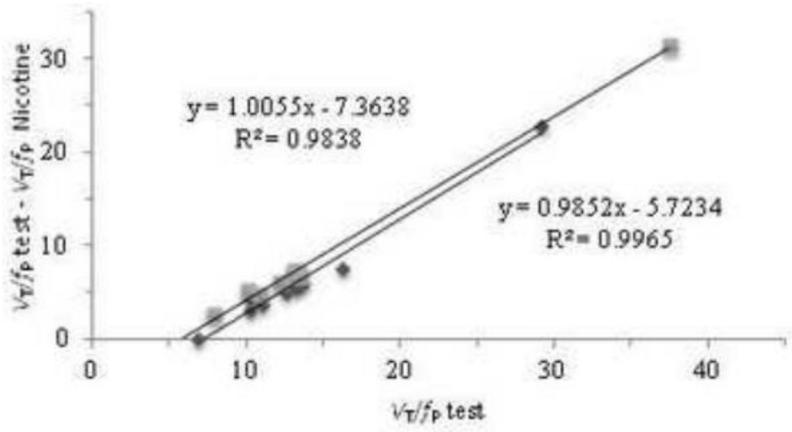


**Figure 5.**

[$^{18}$F]-(−)-NCFHEB occupancy plots after nicotine blockade in two different animals: scatterplot of changes in $V_T/f_P$ between [$^{18}$F]-(−)-NCFHEB baseline scans (average of test and retest scans) and nicotine block scans vs. baseline $V_T/f_P$ in nine regions. The slope of the regression is the estimated occupancy of nicotinic receptors by nicotine, and the x-intercept is the estimated non-specific volume of distribution $V_{ND}/f_P$.

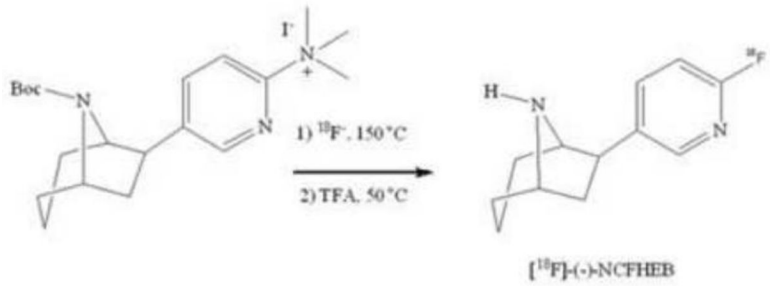


**Scheme 1.**
Radiosynthesis of [$^{18}$F]-(−)-NCFHEB

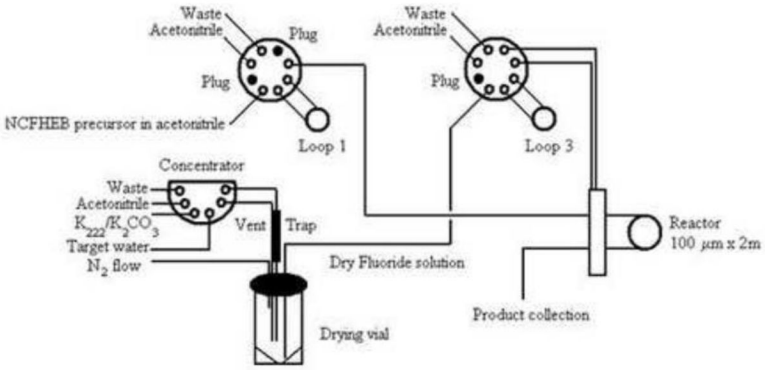


**Scheme 2.**

Schematic drawing of the Advion NanoTek unit used for the radiolabeling of [$^{18}$F]-(−)-NCFHEB

**Table 1**

Regional MA1 $V_T$, $V_T/f_P$ and $BP_{ND}$ values of [$^{18}$F]-(−)-NCFHEB from baseline and blocking scans.

| | Brain Region | | | | | | | | |
|---|---|---|---|---|---|---|---|---|---|
| **Condition** | **Thalamus** | **Front cortex** | **Occipital cortex** | **Temporal cortex** | **Hippocampus** | **Caudate** | **Putamen** | **Cerebellum** | **Brainstem** |
| | $V_T$ | | | | | | | | |
| Baseline | 29 ± 4.9 | 13 ± 1.7 | 9.2 ± 1.0 | 11.1 ± 1.0 | 12 ± 1.0 | 10.5 ± 2.0 | 11.3 ± 1.6 | 6.4 ± 1.0 | 8.9 ± 0.7 |
| Nicotine blocking | 5.8 ± 0.1 | 7.8 ± 0.1 | 6.5 ± 0.1 | 7.0 ± 0.1 | 7.0 ± 0.2 | 6.5 ± 0.2 | 6.7 ± 0.1 | 6.2 ± 0.1 | 5.3 ± 0.1 |
| | $V_T/f_P$ | | | | | | | | |
| Baseline | 33 ± 5.5 | 15 ± 1.9 | 10.5 ± 1.1 | 12.7 ± 1.2 | 13 ± 1.1 | 12.1 ± 2.2 | 12.9 ± 1.7 | 7.4 ± 1.1 | 10.2 ± 0.8 |
| Nicotine blocking | 6.1 ± 0.1 | 6.7 ± 0.1 | 6.1 ± 0.1 | 6.1 ± 0.1 | 6.2 ± 0.1 | 5.8 ± 0.1 | 6.2 ± 0.1 | 5.3 ± 0.1 | 4.9 ± 0.1 |
| | $BP_{ND}$ | | | | | | | | |
| Baseline | 4.1 ± 1.5 | 1.2 ± 0.2 | 0.60 ± 0.33 | 0.91 ± 0.25 | 1.0 ± 0.30 | 0.84 ± 0.54 | 0.96 ± 0.45 | 0.10 ± 0.29 | 0.53 ± 0.25 |

**Table 2**

Test-Retest variability of regional MA1 $V_T$ and $V_T/f_P$ values of [$^{18}$F]-(−)-NCFHEB.

| | Brain Region | | | | | | | | |
|---|---|---|---|---|---|---|---|---|---|
| | **Thalamus** | **Front cortex** | **Occipital cortex** | **Temporal cortex** | **Hippocampus** | **Caudate** | **Putamen** | **Cerebellum** | **Brainstem** |
| $V_T$ | 10% | 13% | 15% | 13% | 13% | 20% | 18% | 18% | 12% |
| $V_T/f_P$ | 12% | 10% | 12% | 10% | 11% | 18% | 16% | 16% | 11% |